


Non-Abelian Berry phase for semiconductor heavy holes under the coexistence of Rashba and Dresselhaus spin-orbit interactions

Tatsuki Tojo^{✉*} and Kyozauro Takeda^{✉†}*Faculty of Science and Engineering, Waseda University, Shinjuku, Tokyo 169-8555, Japan* (Received 16 February 2023; revised 17 August 2023; accepted 5 September 2023; published 26 September 2023)

We formulate the non-Abelian Berry connection (tensor \mathbb{R}) and phase (matrix $\mathbf{\Gamma}$) for a multiband system and apply them to semiconductor holes in the presence of Rashba and Dresselhaus spin-orbit interactions (SOIs). For this purpose, we focus on heavy-mass holes confined in a SiGe two-dimensional quantum well, whose electronic structure and spin texture are explored by the extended $\mathbf{k} \cdot \mathbf{p}$ approach. To explore the influence of the nonadiabatic process, we perform the contour integral of \mathbb{R} faithfully along the equienergy surface by combining the time-dependent Schrödinger equation with the semiclassical equation of motion for a cyclotron and then calculate the energy dependence of $\mathbf{\Gamma}$ computationally. The intersubband interactions in the valence band strongly modifies the SOIs. Accordingly, holes conserve the spin quasidegeneracy at several specific points, where the interstate hybridization generates off-diagonal components both of \mathbb{R} and $\mathbf{\Gamma}$, and the simple π quantization found in the Abelian Berry phase is violated. Moreover, these off-diagonal terms cause “resonant repulsion” at the quasidegenerate energy. Consequently, $\text{HH}\pm$ exhibits a discontinuity in the energy dependence of $\mathbf{\Gamma}$.

DOI: [10.1103/PhysRevB.108.125432](https://doi.org/10.1103/PhysRevB.108.125432)

I. INTRODUCTION

Recent intensive studies coupled with physicomathematics [1–3] have provided novel interpretations of the unusual quantum phenomena discovered in graphene [4–7]. Then, a novel perspective “topology” was born in condensed matter physics. The representative for identifying materials’ topology is Berry parameters (connection, curvature, and phase) [8] and/or Chern number [9]. In fact, Novoselov *et al.* [5] and Zhang *et al.* [10] confirmed the relevance of Berry’s phase to an unusual half-integer quantum Hall effect by observing magneto-oscillations in graphene. Physicomathematics further reveals that two types of symmetry breaking cause topological features in materials via spin-orbit interaction (SOI). These symmetry breakings are the structure-inversion-asymmetry (SIA) and bulk-inversion-asymmetry (BIA), causing Rashba(R)- [11] and Dresselhaus(D)-type [12] SOI, respectively. Thus electrons and holes having a simple Dirac- or Weyl-type Hamiltonian have been intensively and extensively studied both from experiments and theories [20].

The addition of spatial asymmetry naturally causes SOIs for holes in three-dimensional (3D) bulk semiconductors because of the finite angular momentum ($|\ell| = 1$). Consequently, a k -linear (or odd) term appears in the dispersion relation, and the spin degeneracy is fully resolved in the Brillouin zone (BZ), except at the center point Γ [13,14]. However, this finite value $|\ell| = 1$ produces a complicated valence band comprising three types of subbands: heavy-mass (HH), light-mass (LH), and split-off (SoH) holes. The existence of these subbands inevitably causes a strong in-

tersubband interaction (ISI), which produces anisotropy and nonparabolicity in the valence band \mathcal{E} - \mathbf{k} dispersion relation. This valence-band complexity makes it difficult to deeply understand the peculiar SOI- and spin-related quantum phenomena originating from the hole topology, leading to a few previous studies. Winkler and his group pioneered studies on holes’ SOI-related phenomena by refining the \mathcal{E} - \mathbf{k} dispersion via the appropriate removal of warping and anisotropy [15–19].

Considering the above background, ISI is expected to cause unusual quantum phenomena in holes. To comprehend these peculiar quantum phenomena originating from the valence band topology, it is necessary to revert to a fundamental understanding of topological parameters, such as Berry’s connection, curvature, and phase. Therefore we focused on HHs in a SiGe two-dimensional quantum well (2DQW) and studied the Berry parameters using numerical calculations [8,13,14]. The application of our extended $\mathbf{k} \cdot \mathbf{p}$ approach to SiGe 2DQW reveals that the SOI owing to the BIA coupled strongly with the ISI produces the quasidegenerate states at specific points in the $\langle 100 \rangle$ direction. It also shows that the SOI by the SIA couples strongly with the ISI and causes the quasidegenerate states at specific points in the $\langle 110 \rangle$ direction. Of interest is that these plural quasidegenerate points remain even in the 2DQW system and that these quasidegenerate points generate a complicated distribution of the effective magnetic field, such as vortices, sources, and sinks, leading to characteristic spin textures [13,14,20].

However, our previous calculation of Berry’s parameters appears to be one-sided because the treatment was performed while considering an adiabatic process. Despite the small energy difference between the quasidegenerate states, we ignored the intersubband transition. It is necessary to consider the influence of the nonadiabatic process via intersubband

*tojo@qms.cache.waseda.ac.jp

†takeda@waseda.jp

hybridization and revisit the fundamental Berry's parameters. We first formulate the non-Abelian Berry connection (tensor \mathbb{R}) and phase (matrix Γ) for a multiband system (Sec. II). Several pioneering studies have been conducted on the non-Abelian treatment of Berry's analysis, which have deepened our understanding [21–23] in the field of the quantum information and computation [24–27]. Here, we develop non-Abelian formulation in conformity with the practical subject of semiconductor holes, while sacrificing mathematical strictness, because we intend to apply our formulation to semiconductor holes having complicated electronic structures and spin textures owing to the coexistence of R- and D-type SOIs (Sec. III). Thus we focus on HHs confined in a SiGe 2DQW and then calculate the energy dependence of Γ computationally by performing the contour integral of \mathbb{R} faithfully along the equienergy surface by combining the time-dependent (TD) Schrödinger equation with the semiclassical equation of motion for a cyclotron (Sec. III C).

II. THEORETICAL TREATMENT FOR NON-ADIABATIC PROCESSES

A. Non-Abelian Berry connection tensor

The Berry phase is the phase difference of the wave function and is defined by the contour integral when the final state becomes identical to the initial state during the specific motion characterized by the parameters used to describe the system accurately. As we are investigating the Berry phase of the carrier having a Bloch state, we can use a wave vector \mathbf{k} as the parameter that describes the system well. We define the periodic part of the n th Bloch eigenstate as $|u_k^n\rangle$. Thus any state $|\phi_k\rangle$ of the carrier is represented by the expansion of $|u_k^n\rangle$ because of the completeness at \mathbf{k} :

$$|\phi_k\rangle = \sum_n c_k^n |u_k^n\rangle, \quad (1)$$

where n represents the spin polarization (α and β) as well as the n th band index.

We now explore the \mathbf{k} -space trajectory, the final state \mathbf{k}_f of which returns to the initial state \mathbf{k}_i . The equienergy surface is representative of this trajectory, which is realized by the ‘‘cyclotron motion.’’ Thus we recreate the ‘‘dynamical’’ process of the carrier via the cyclotron motion, the TD feature of which is described by the semiclassical equation of motion. This recreation via the cyclotron motion enables us to solve the time dependence of the wave vector by coupling the semiclassical equation of motion with the TD Schrödinger equation. Accordingly, we can implicitly include the time dependence in the projection coefficient c_k^n in Eq. (1), although the wave vector \mathbf{k} does not originally comprise a time-dependence term. In addition, energy conservation during the cyclotron motion results in the following physical insights. The adiabatic process specifically determines the equienergy surface of the single eigenstate $|u_k^n\rangle$. Consequently, the closed trajectory with $\mathbf{k}_i = \mathbf{k}_f$ is naturally and uniquely determined by the single-cycle motion. In contrast, the nonadiabatic process allows the carrier to cause interstate hybridization, even during the cyclotron motion, along the energy-conserved \mathbf{k} -space trajectory. The resulting \mathbf{k} -space trajectory cannot be represented by the single equienergy surface of the specific eigenstate

but by synthesizing multi-equienergy surfaces because the carrier switches between multiple states. Thus the single-cycle cyclotron motion in the nonadiabatic process does not always equalize the final wave vector \mathbf{k}_f to the initial one \mathbf{k}_i . Multicycle cyclotron motion is possibly required to realize the closed trajectory of $\mathbf{k}_i = \mathbf{k}_f$.

Using Eq. (1), we rewrite the TD Schrödinger equation

$$i\hbar \frac{d}{dt} |\phi_k(t)\rangle = \hat{H}_k |\phi_k(t)\rangle, \quad (2)$$

into the following rate equation:

$$\begin{aligned} \frac{dc_k^m}{dt} &= -\sum_{m'} \left(\sum_{\xi} \left\langle u_k^m \left| \frac{\partial u_k^{m'}}{\partial k_{\xi}} \right. \frac{dk_{\xi}}{dt} \right\rangle c_k^{m'} - i \frac{E_k^m}{\hbar} c_k^m \right) \\ &= i \sum_{m'} \left(\sum_{\xi} \mathbb{R}_{mm'}^{\xi}(\mathbf{k}) \dot{k}_{\xi} \right) c_k^{m'} - i \frac{E_k^m}{\hbar} c_k^m. \end{aligned} \quad (3)$$

Here, the normalized orthogonality $\langle u_k^m | u_k^{m'} \rangle = \delta_{mm'}$ results in the relation

$$\left\langle \frac{du_k^m}{dt} \left| u_k^{m'} \right. \right\rangle = - \left\langle u_k^m \left| \frac{du_k^{m'}}{dt} \right. \right\rangle. \quad (4)$$

In Eq. (3), we further define a tensor component $\mathbb{R}_{mm'}^{\xi}(\mathbf{k})$ as follows:

$$\mathbb{R}_{mm'}^{\xi}(\mathbf{k}) = i \left\langle u_k^m \left| \frac{\partial u_k^{m'}}{\partial k_{\xi}} \right. \right\rangle. \quad (5)$$

Because we are studying a 2D system herein, we focus on the in-plane components $\xi = x$ and y . This procedure does not eliminate the generality of the formulation (5).

The tensor $\mathbb{R}_{mm'}^{\xi}(\mathbf{k})$ defined by Eq. (5) is mathematically equivalent to the Berry connection tensor. From the physical perspective, this tensor is the non-Abelian Berry connection for the nonadiabatic process [22,28] because the interstate hybridization between $|u_k^m\rangle$ and $|u_k^{m'}\rangle$ is taken into consideration. The noncommutativity of the non-Abelian Berry connection tensor appears explicitly in the time-ordered product in the calculation of the Berry phase matrix.

The diagonal term ($m' = m$) of Eq. (5) is given by

$$\mathbb{R}_{mm}^{\xi}(\mathbf{k}) = i \left\langle u_k^m \left| \frac{\partial u_k^m}{\partial k_{\xi}} \right. \right\rangle \equiv A_m^{\xi}(\mathbf{k}). \quad (6)$$

The symbol $A_m^{\xi}(\mathbf{k})$ is the ξ component of the Abelian Berry connection vector $\mathbf{A}_m(\mathbf{k})$ for the m th carrier, which is given by

$$\mathbf{A}_m(\mathbf{k}) = i \langle u_k^m | \nabla_k | u_k^m \rangle. \quad (7)$$

B. Non-Abelian Berry phase matrix

To eliminate the dynamical phase from $\mathbb{R}_{mm'}^{\xi}(\mathbf{k})$, we further redefine the rationalized Berry connection tensor $\mathbb{R}^{\xi}(\mathbf{k})$ as follows:

$$\begin{aligned} \mathbb{R}^{\xi}(\mathbf{k}) &= \left(\exp \left[i \int_0^t \mathbf{\Xi}_{k(t')} dt' / \hbar \right] \right) \mathbb{R}^{\xi}(\mathbf{k}) \\ &\quad \times \left(\exp \left[-i \int_0^t \mathbf{\Xi}_{k(t')} dt' / \hbar \right] \right). \end{aligned} \quad (8)$$

Here, we introduce the energy eigenvalue matrix $\Xi_{\mathbf{k}}$, the diagonal elements of which are the eigenvalues of the Bloch eigenstates:

$$\Xi_{\mathbf{k}} = \begin{pmatrix} E_{\mathbf{k}}^1 & & \mathbf{0} \\ & E_{\mathbf{k}}^2 & \\ \mathbf{0} & & \ddots \end{pmatrix}. \quad (9)$$

Accordingly, when a “time” $t = T_{\text{cls}}$ passes, and the final point $\mathbf{k}_f(E)$ becomes the initial point $\mathbf{k}_i(E)$ ($t = 0$), we have the non-Abelian Berry phase matrix $\Gamma(E)$ [21,22]:

$$\begin{aligned} \Gamma(E) &= -\frac{i}{N_{\text{cyc}}} \ln \left(\mathcal{T} \exp \left[i \sum_{\xi} \int_0^{T_{\text{cls}}} \mathbb{R}^{\xi} \dot{k}_{\xi}(E) dt \right] \right) \\ &= -\frac{i}{N_{\text{cyc}}} \ln \left(\mathcal{T} \exp \left[i \sum_{\xi} \oint_{\mathbf{k}_i(E)}^{\mathbf{k}_f(E)} \mathbb{R}^{\xi} dk_{\xi}(E) \right] \right), \end{aligned} \quad (10)$$

where we define the time derivation of the wave vector \mathbf{k} using the notation $\dot{\mathbf{k}} (= d\mathbf{k}/dt)$, and N_{cyc} is the number of cycles required to form the closed trajectory. We also employ the time-ordered product \mathcal{T} while considering the noncommutativity in the Berry connection tensor $\mathbb{R}^{\xi}(\mathbf{k}(E))$.

If the system is described well by the adiabatic approximation, the off-diagonal elements (noncommutative) of the Berry connection \mathbb{R} are negligible, which results in a diagonal Berry connection $\mathbf{R}_{mm} (= \mathbf{A}_m)$. Accordingly, \mathbb{R} at any time is commutative, and the time-ordered product simply offsets the mathematical operations “ln” and “exp” in Eq. (10). Consequently, Stokes’ theorem transforms the contour integral to the surface integral as follows:

$$\begin{aligned} \Gamma(E) &= -\frac{i}{N_{\text{cyc}}} \ln \left(\exp \left[i \oint_{\mathbf{k}_i(E)}^{\mathbf{k}_f(E)} \mathbb{R} \cdot d\mathbf{k}(E) \right] \right) \Rightarrow \oint_E \mathbf{R} \cdot d\mathbf{k} \\ &= \iint_{\leq E} \nabla \times \mathbf{R} dk_x dk_y. \end{aligned} \quad (11)$$

C. Cyclotron motion

To calculate the non-Abelian Berry phase, we must perform the contour integral in Eq. (10) by focusing attention on the time-ordered product caused by the noncommutativity of the non-Abelian Berry connection. In addition, we are required to describe the “time dependence” of the wave vector because the integrand has the term $\dot{\mathbf{k}}$. Here, we focus on the magnetic field $\mathbf{B}_0 = (0, 0, B_0)$ applied to resolve the spin degeneracy. This field causes a “cyclotron motion,” using which we can alter the motion of the wave vector to follow the \mathbf{k} trajectory. The semiclassical equation of motion describes this TD feature as follows:

$$\frac{d\mathbf{k}}{dt} = \frac{q}{\hbar^2} \langle \phi_{\mathbf{k}} | \nabla_{\mathbf{k}} \hat{\mathcal{H}}_{\mathbf{k}} | \phi_{\mathbf{k}} \rangle \times \mathbf{B}_0. \quad (12)$$

Accordingly, the coupling of Eqs. (3) and (12) enables us to perform the contour integral accurately along the cyclotron \mathbf{k} trajectory by taking into consideration the time-ordered product in Eq. (10).

III. APPLICATION TO SIGE BINARY ALLOY SYSTEM

A. Electronic structure and spin texture

Here, we have extended the $\mathbf{k} \cdot \mathbf{p}$ approach of Dresselhaus, Kip, and Kittel (hereafter, abbreviated DKK) [29] by considering the crossings between the $\mathbf{k} \cdot \mathbf{p}$ and R- or D-SOI coupling up to the second-order terms. We, then, applied it to SiGe 2DQW system and studied the spin textures of the R- and D-SOI competition system [13,14]. The extended $\mathbf{k} \cdot \mathbf{p}$ approach can be used to determine both the periodic part $|u_{\mathbf{k}}^n\rangle$ and eigen energy $E_{\mathbf{k}}^n$ of the n th Bloch hole $|\varphi_{\mathbf{k}}^n(\mathbf{r})\rangle = e^{i\mathbf{k} \cdot \mathbf{r}} |u_{\mathbf{k}}^n(\mathbf{r})\rangle$ precisely while taking into consideration the ISI:

$$\begin{aligned} \hat{\mathcal{H}}_{\mathbf{k}}^{\text{exd}} |u_{\mathbf{k}}^n\rangle &= (\hat{\mathcal{H}}_0 + \hat{\mathcal{H}}'_{\mathbf{k}} + \mu_B \hat{\sigma} \cdot \mathbf{B}_0) |u_{\mathbf{k}}^n\rangle \\ &= \left(E_{\mathbf{k}}^n - \frac{\hbar^2 k^2}{2m} \right) |u_{\mathbf{k}}^n\rangle \equiv \mathcal{E}_{\mathbf{k}}^n |u_{\mathbf{k}}^n\rangle. \end{aligned} \quad (13)$$

Here, $\hat{\mathcal{H}}_0$ is the nonperturbed Hamiltonian, and $\hat{\mathcal{H}}'_{\mathbf{k}}$ is the extended $\mathbf{k} \cdot \mathbf{p}$ Hamiltonian given by

$$\begin{aligned} \hat{\mathcal{H}}'_{\mathbf{k}} &= \hat{\mathcal{H}}'_{\mathbf{k} \cdot \mathbf{p}} + \hat{\mathcal{H}}'_{\text{cSOI}} + \hat{\mathcal{H}}'_{\text{SIAk}} + \hat{\mathcal{H}}'_{\text{SIAp} \otimes \mathbf{k} \cdot \mathbf{p}} + \hat{\mathcal{H}}'_{\text{BIAk}} \\ &\quad + \hat{\mathcal{H}}'_{\text{BIAp} \otimes \mathbf{k} \cdot \mathbf{p}}. \end{aligned} \quad (14)$$

Here, $\hat{\mathcal{H}}'_{\mathbf{k} \cdot \mathbf{p}}$ is the DKK second-order $\mathbf{k} \cdot \mathbf{p}$ perturbation Hamiltonian, and $\hat{\mathcal{H}}'_{\text{cSOI}}$ is the internal SOI perturbed Hamiltonian caused by the crystal potential (corresponding to so-called $\ell \cdot s$ coupling) [29]. The remaining four terms in Eq. (14) correspond to the SOI terms that are related to the SIA and BIA, as defined in our previous work [30,31]. Eventually, we have diagonalized the extended $\mathbf{k} \cdot \mathbf{p}$ Hamiltonian $\hat{\mathcal{H}}_{\mathbf{k}}^{\text{exd}}$ of 6×6 matrix. We have already reported the formulation of the above extended $\mathbf{k} \cdot \mathbf{p}$ approach [13,30]. The essence of the perturbed Hamiltonians is summarized in Ref. [32].

In this calculation, the holes are assumed to be confined in the $\text{Si}_{0.5}\text{Ge}_{0.5}$ 2DQW system, which has an alternating configuration and where the BIA is the most strengthened [47,48]. We apply a Rashba electric field perpendicular (z) to the (001) quantum plane (xy) to study the SIA-BIA coexistence system [14,49–53]. We also consider 2D quantization by employing the conventional approach of $\langle k_z \rangle = 0$ and $\langle k_z^2 \rangle = (\pi n_z / L_z)^2$, where L_z and n_z are the quantum plane thickness and z -directional quantum number, respectively, [54]. Of a remark is that the competition between the internal SOI and 2D quantization changes the valence band structure of the 2DQW from that of the 3D bulk. The 2D system enables us to classify holes based on their in-plane (xy) and out-of-plane (z) symmetry characteristics. We demonstrated that the former in-plane holes have two characteristics analogous to conventional HH and LH. We further revealed that 2D quantization destabilizes the out-of-plane hole energetically, *separating* it from HH and LH using internal SOI coupling. As such, we refer to this third hole as a separate hole (SH) because it has an electronic feature resembling that of an SoH of the 3D bulk system but is not always equal to SoH (Ref. [32]).

The 2DQW system considered herein has a thickness of 41 atomic layers to incorporate the BIA characteristics straightforwardly. This thickness separates the first excited states of these three types of holes from their ground states (at least 140 meV). Accordingly, the ground state is crucial for the

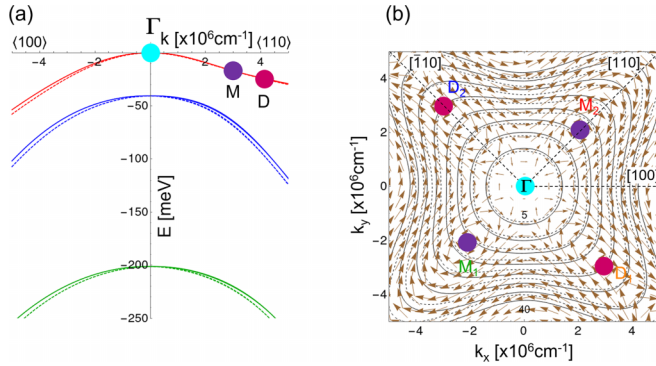


FIG. 1. \mathcal{E} - k dispersion relation (a), and spin texture (vector field) with equienergy contours (b) of the 2DQW system, consisting of the $\text{Si}_{0.5}\text{Ge}_{0.5}$ alternating alloy. The system comprises the (001) quantum plane, and the SIA and BIA couplings have an equivalent strength [14]. The \mathcal{E} - k dispersion relations of the HHs, LHs, and SHs are indicated in red, blue, and green, respectively; the solid and broken lines represent states with a stabilized spin (+) and destabilized spin (−), respectively. We present the equienergy contours of $\text{HH}\pm$ with an energy interval of 5 meV (b). The colored circles in the figures indicate the quasidegenerate points between $\text{HH}\pm$. We illustrate the norm value of the in-plane vector by the arrow length in a logarithmic scale. All the \mathcal{E} - k dispersions (a) and equienergy surfaces (b) are those of the ground state against the 2D quantization. [These figures are reproduced from our previous work [14] and partly modified. Copyright (2022) by Wiley-VCH GmbH.]

present consideration. The influence of the excited states is negligible in this non-Abelian analysis because an interesting feature in the non-Abelian Berry phases arises in the region with energies less than 20 meV, as mentioned in Sec. III C. The details of the Hamiltonian formulation and calculations are summarized in Ref. [32], respectively.

Figure 1(a) presents the ground-state \mathcal{E} - k dispersion relations of the three types of holes confined in the $\text{Si}_{0.5}\text{Ge}_{0.5}$ 2DQW system under the SIA–BIA coexistence [13]. As the SOIs caused by the Rashba and Dresselhaus couplings stabilize(+)/destabilize(−) each type of hole, we indicate them using solid/broken lines, respectively. We then present the corresponding equienergy contours and spin texture of $\text{HH}\pm$ in Fig. 1(b). The ISI causes strong anisotropy and nonparabolicity in both $\text{HH}+$ and $\text{HH}-$ toward the $\langle 110 \rangle$ directions, resulting in quasidegeneracy between $\text{HH}\pm$, as found in Figs. 1(a) and 1(b). The C_2 symmetry of the system results in two pairs of the quasidegenerate points: M_1 and M_2 in the $[\bar{1}\bar{1}0]$ and $[110]$ directions, respectively, and D_1 and D_2 in the $[1\bar{1}0]$ and $[\bar{1}10]$ directions, respectively. A definite spin-vortex results around point M , while the spin distribution spreads characteristically in the $\langle 1\bar{1}0 \rangle$ direction, and the resulting vortex around point D is comparatively indistinct.

B. Non-Abelian Berry connection

By employing the eigenvector $|u_k^n\rangle$, we calculate the non-Abelian Berry connection \mathbb{R} based on Eq. (5) and present the distribution of the in-plane component in the vector-field representation in Fig. 2(a). The Berry connection \mathbb{R} is *gauge variant*. However, we herein execute the contour integration faithfully along the closed loop of the Berry connection

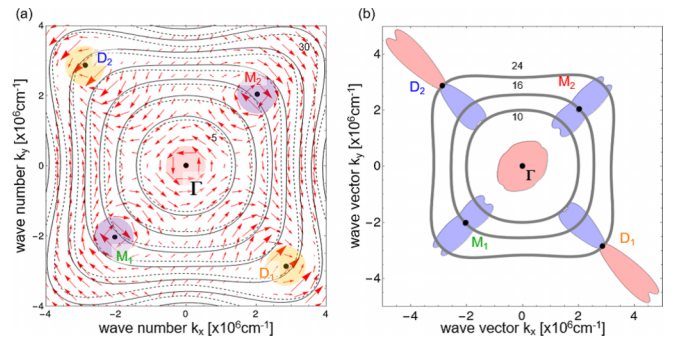


FIG. 2. Vector-field representation of the in-plane vector of the non-Abelian Berry connection with the equienergy surfaces (a). We illustrate the norm value of the in-plane vector by the arrow length in a logarithmic scale. We present the distribution of the Abelian Berry curvature of $\text{HH}+$ in (b); the negative values are indicated in blue while the positive ones are in red. [(b) is reproduced from our previous works [13,14] and partly modified. Copyright (2020) by Elsevier B.V., (2022) by Wiley-VCH GmbH.]

and estimate the non-Abelian Berry phase (*gauge invariant*). Therefore the distribution of \mathbb{R} deepens our understanding on the feature of the contour integral, especially an energy dependence of the non-Abelian Berry phase.

In the lower-energy region around the point Γ , the in-plane component vector is concentrically distributed with an anti-clockwise rotation. It is also characteristic that the norms of the in-plane vectors are uniform. This feature remains as long as the energy is less than 5 meV. However, when the energy is greater than 5 meV, the in-plane component is weakened in the $\langle 100 \rangle$ direction but strengthened in the $\langle 110 \rangle$ direction. As such, the uniform concentric-distribution breaks.

The nonuniform distribution thus obtained results in the characteristic vector-field of the non-Abelian Berry connection. Particularly around the quasidegenerate point M at 16 meV, a vortex of the non-Abelian Berry connection is observed. Furthermore, with an increase in energy, the in-plane component decreases in the $\langle 110 \rangle$ direction and increases in the $\langle 1\bar{1}0 \rangle$ direction. However, a vortex is not observed at the other quasidegenerate point D ; the non-Abelian Berry connection strengthens its own in-plane component maximally. Eventually, with a further increase in energy, the in-plane component is reduced, even in the direction of $\langle 1\bar{1}0 \rangle$. Thus the resulting vector-field has a complicated distribution with a change in energy; the direction of the in-plane vector in $\langle 110 \rangle$ is opposite to that in $\langle 1\bar{1}0 \rangle$. Nevertheless, the total vector-field has a C_2 rotational symmetry.

C. Non-Abelian Berry phase

While employing the non-Abelian Berry connection \mathbb{R} , we explore the Berry phase Γ for $\text{HH}\pm$ beyond the adiabatic process. In the practical calculation, we set the initial state of the considered hole $|\phi_k\rangle$ to the eigen state of $\text{HH}+$, having $\mathbf{k}_i^{\text{HH}+} = (k_i^{\text{HH}+}, 0)$, and execute the contour integral along the k -space cyclotron trajectory under energy conservation by coupling the semiclassical equation of motion for the cyclotron motion (12) with the rate equation (3).

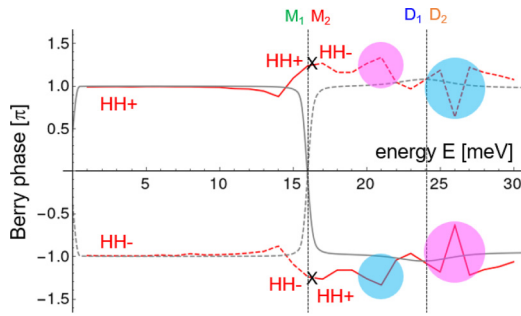


FIG. 3. Energy dependence of the non-Abelian Berry phase for HH+ and HH- beyond the adiabatic approximation. A discontinuity in the non-Abelian Berry phases [red solid (+) and broken (-) lines] is observed at the energy indicated by \times . For the purpose of comparison, we overwrite the corresponding energy-dependence of the Abelian Berry phase (gray lines) [13,14] that is calculated using Eq. (11). [The gray lines are reproduced from our previous works [13,14] and partly modified. Copyright (2020) by Elsevier B. V., (2022) by Wiley-VCH GmbH.]

To obtain the time-ordered product in the integration of Eq. (10), we rewrite the non-Abelian Berry phase matrix using the unitary matrix $U(t)$ as

$$\Gamma(E) = -\frac{i}{N_{\text{cyc}}} \ln[U(T_{\text{cls}})], \quad (15)$$

where the unitary matrix is given by

$$U(t) = \mathcal{T} \exp \left[i \sum_{\xi} \int_0^t \mathbb{R}^{\xi} \dot{k}_{\xi}(E) dt' \right]. \quad (16)$$

On employing the Crank–Nicolson algorithm, we determine the unitary matrix having a short-time proceeding Δt :

$$\begin{aligned} U(t + \Delta t) &= \left(I - i \sum_{\xi} \mathbb{R}^{\xi}(t + \Delta t/2) \dot{k}_{\xi}(t + \Delta t/2) \frac{\Delta t}{2} \right)^{-1} \\ &\times \left(I + i \sum_{\xi} \mathbb{R}^{\xi}(t + \Delta t/2) \dot{k}_{\xi}(t + \Delta t/2) \frac{\Delta t}{2} \right) U(t), \end{aligned} \quad (17)$$

with the initial condition of $U(0) = I$. Thus we have the non-Abelian Berry phase of Eq. (10). We have provided the calculation details in Appendix B 2.

Figure 3 presents the non-Abelian Berry phase versus energy: eigenvalues of $\gamma_{\text{HH}\pm}(E)$. The red solid and broken lines indicate the energy dependence of HH+ and HH-, respectively. The comparison of the non-Abelian Berry phase with the Abelian one reveals the influence of the nonadiabatic process and deepens our understanding of the energy dependence of the Berry phase. For the adiabatic process, we have the Berry curvature as shown in Fig. 2(b). Consequently, by employing Stokes' theorem, we can calculate the Abelian Berry phase using Eq. (11). We give those in Fig. 3 by gray solid (HH+) and broken (HH-) lines.

As in the case of other semiconductors, the present $\text{Si}_{0.5}\text{Ge}_{0.5}$ 2DQW system has a massive Weyl-like singularity at point Γ , and HH \pm has the Berry phase of $\pm\pi$, irrespective of whether an adiabatic or a nonadiabatic process is considered. Thus the non-Abelian Berry phase $\gamma(E)$ for HH \pm also converges into $\pm\pi$ toward the top of the valence band, as observed in Fig. 3. For the Abelian Berry phase in the adiabatic process, HH \pm maintains the value $\pm\pi$ until the quasidegenerate points M_1 and M_2 newly appear. In the lower-energy region, with an energy of less than ~ 10 meV, the nonadiabatic process results in almost no change in the energy dependence of $\gamma(E)$ from that observed in the adiabatic process, i.e., the nonadiabatic process exhibits a similar plateau profile with $\gamma_{\text{HH}\pm}(E) = \pm\pi$.

The Abelian Berry curvature around point M is negative [Fig. 2(b)], and the surface integral provides the Berry phase of $-\pi$ (Fig. 3). As this feature is similar to the conventional massive Dirac fermion [55], we refer to point M as a “monopole.” Consequently, the monopole-like singularity changes the Abelian Berry phase from $\pm\pi$ to $\mp\pi$ for HH \pm at the quasidegenerate energy. However, the nonadiabatic process causes an unexpected change in the sign of the Berry phase and produces a *discontinuity* in $\gamma(E)$ owing to the mutual interchange between HH \pm . This feature is completely different from the abrupt but continuous change in the sign of the Berry phase observed in the case of the adiabatic process. Figure 2(b) also shows that the Berry curvature exhibits a change in its sign from negative to positive at point D with an increase in energy. The surface integral around point D results in a “zero” Berry phase. Accordingly, point D possibly has a “dipole” character and has less influence on the Abelian Berry phase [13,14]. In contrast, the nonadiabatic process results in a characteristic “bumpy” profile that is different from the flat profile ($\gamma = \mp\pi$) in the adiabatic process.

1. In the lower energy region

Here, we explore the non-Abelian Berry phase $\gamma(E)$ up to ~ 10 meV. Figure 4(a) presents the vector field of the non-Abelian Berry connection. We also illustrate the \mathbf{k} trajectory owing to the cyclotron motion while overwriting the equienergy surfaces of HH \pm with 10 meV. The cyclotron motion trajectory completely coincides with the equienergy surface of HH+. Moreover, the final position \mathbf{k}_f of the hole $|\phi_{\mathbf{k}}\rangle$ accurately returns to the initial position \mathbf{k}_i owing to the single-cycle motion. The projection analysis reveals that the hole $|\phi_{\mathbf{k}}\rangle$ consists primarily of HH+, and few states are hybridized even under the nonadiabatic process during the cyclotron motion. Accordingly, the \mathbf{k} -space trajectory coincides with the HH+ equienergy surface of 10 meV [Fig. 4(b)].

Figure 4(c) presents the successive integration (red line) of the inner product between the Berry connection \mathbb{R} and the time-derivative of the wave vector $\dot{\mathbf{k}}$. We perform integration stepwise until time t along the cyclotron trajectory. Any intermediate values obtained are *gauge variant* and physically meaningless, with the exception of the full contour integral. However, the “midway” integrals explain the determination process of the Berry phase well. Figure 4(a) demonstrates that the non-Abelian Berry connection results in the large values in the $\langle 110 \rangle$ and $\langle \bar{1}\bar{1}0 \rangle$ directions. Moreover, these connection

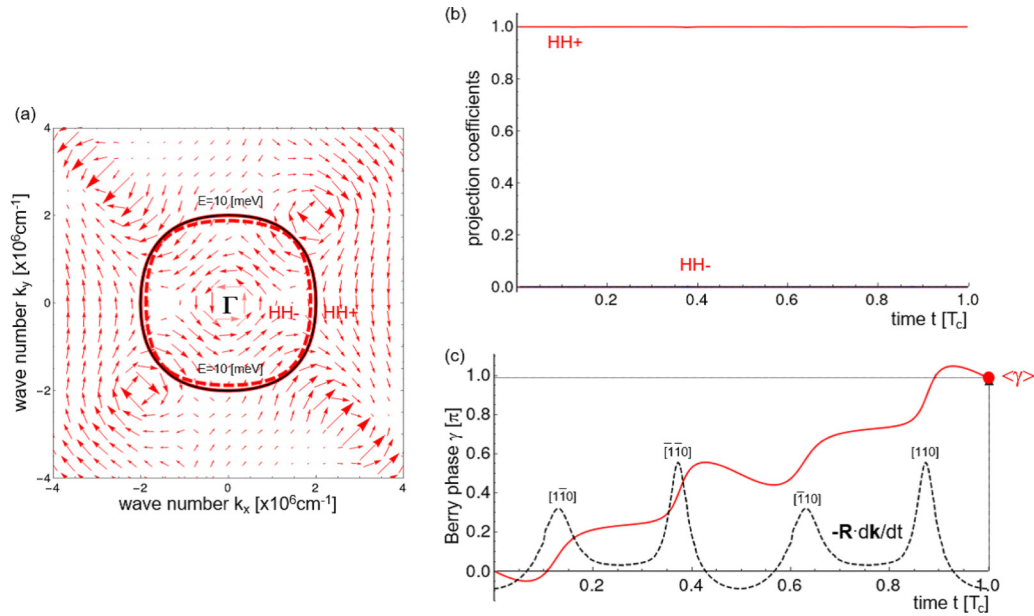


FIG. 4. k -space trajectory (black solid line) of the hole having an energy of 10 meV (a). We illustrate the vector-field distribution of the non-Abelian Berry connection (red arrows) for HH+ with the equienergy surfaces (10 meV) of HH+ (red solid line) and HH- (red broken line). We illustrate the norm value of the in-plane vector by the arrow length in a logarithmic scale. We present the projection profile (b), and the successively integrated values (red line) of the inner product (black broken line) between \mathbb{R} and $\hat{\mathbf{k}}$ (c).

vectors are antiparallel to the cyclotron direction of the hole having an energy of 10 meV. Consequently, the absolute value of an inner product between \mathbb{R} and $\hat{\mathbf{k}}$ increases stepwise at every point at which the hole crosses the aforementioned four directions [broken line in Fig. 4(c)]. Except in the case of the aforementioned four directions, the value of the Berry connection vector is small, and a small inner-product value is obtained. It should be noted that the C_2 rotational symmetry of the system lets the hole repeat the same TD profile when the time equals half the cycle time $T_c (= T_{\text{cls}}/N_{\text{cyc}})$. In such a manner, the hole in the nonadiabatic process undergoes these complicated *gauge-variant* processes. Nevertheless, the non-Abelian Berry phase γ determined by the contour integral coincides with the value obtained under the adiabatic process. That is, the non-Abelian Berry phase of HH+ (and HH-) up to ~ 10 meV is well described by the adiabatic approximation.

2. At the “monopole” point M

We explore how the non-Abelian Berry phase is affected when the hole passes the quasidegenerate points M_1 and M_2 . For this purpose, we set the hole initially with the HH+ eigenstate having 16 meV. The resulting \mathbf{k} trajectory and projection coefficients are presented in Figs. 5(a) and 5(b), respectively. The hole first exhibits a \mathbf{k} trajectory (black solid line) equal to the equienergy surface of HH+ (red solid line) because the hole initially has the HH+ eigenstate. Figure 5(b) demonstrates that the hole changes from HH+ to HH- when it passes point M_1 . Accordingly, the hole also changes the trajectory from the equienergy surface of HH+ (red solid line) to that of HH- (red broken line). The C_2 symmetry of the system further results in a transition back to HH+ at the quasidegenerate point M_2 . The trajectory returns to the equienergy surface of HH+, and the closed trajectory having

$k_i = k_f$ is inevitably realized owing to the single cyclotron cycle. Thus the hole alternates between the HH \pm states when it passes the “monopole” points M_1 and M_2 and goes back and forth over the two equienergy surfaces of HH \pm during the cyclotron motion owing to the conservation of energy.

The nonadiabatic process allows the interstate transition and then induces the off-diagonal terms $\mathbb{R}_{mm'}^\xi(\mathbf{k})$. Consequently, the non-Abelian Berry connection vector has a characteristic distribution comprising a vortex at the quasidegenerate point M , as shown in Fig. 5(a). This off-diagonal Berry connection element $\mathbb{R}_{mm'}^\xi(\mathbf{k})$ further induces the off-diagonal terms of the non-Abelian Berry phase matrix Γ . Figure 6 illustrates the energy dependence of the diagonal (a) and off-diagonal (b) elements of Γ for HH \pm around the quasidegenerate point M . The absolute value of the diagonal element decreases and becomes zero at point M . These diagonal terms then cross mutually and increase. The energy profiles of these diagonal elements resemble those of the Abelian Berry phases (Fig. 3), wherein the adiabatic process prohibits interstate hybridization. In contrast, the nonadiabatic process causes the off-diagonal terms to reach a maximum at point M [Fig. 6(b)]. That is, the intercrossing of the Abelian Berry phases at point M changes into the “avoid crossing” by the off-diagonal elements which are caused by the interstate transition via the nonadiabatic process. This “resonant repulsion” causes discontinuity in the non-Abelian Berry phases for HH \pm at the quasidegenerate point M (Fig. 3). Moreover, the interstate transition breaks the rigorous π quantization.

We investigate what happens when the cyclotron trajectory is slightly away from point M . Figure 7 presents the \mathbf{k} trajectory (a), the projection coefficients (b), and their Fourier analysis (c) for the hole having an energy of 15 meV. The further away the cyclotron trajectory is from point M , the

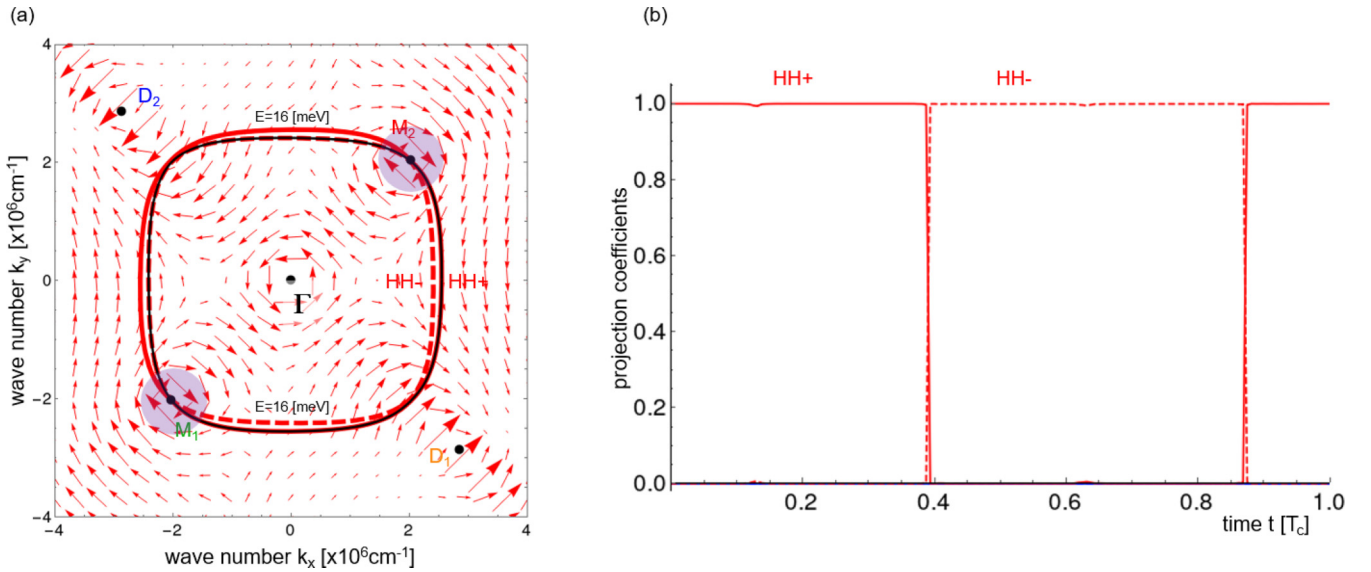


FIG. 5. k -space trajectory (black solid line) of the hole having an energy of 16 meV with the vector-field distribution of the non-Abelian Berry connection (red arrows) and the equienergy surfaces (16 meV) of $HH+$ (red solid line) and $HH-$ (red broken line) (a). We illustrate the norm value of the in-plane vector by the arrow length in a logarithmic scale. We present the projection coefficients $|c_k^m|^2$ vs time (b).

greater the energy difference ΔE^\pm between the $HH\pm$ results, and the interstate transition between $HH\pm$ is reduced. Thus the k trajectory (a) is formed by synthesizing the equienergy surfaces of $HH+$ and $HH-$ having an energy of 15 meV in accordance with the hybridization ratio. The nonadiabatic process results in this complicated interstate transition and requires 80 cyclotron cycles to close the trajectory for $E = 15$ meV. The Fourier analysis [Fig. 7(c)] demonstrates that any peaks are expressed by a rational number with a denominator of 80, because the frequency ratio of the l th harmonics is given by $\omega_l/\omega_c = l/N_{\text{cyc}}$.

3. At the “dipole” point D

We further explore the k trajectory (a) and the projection profile (b) when the hole passes other quasidegenerate points D_1 and D_2 at approximately 24 meV (Fig. 8). Despite the small energy difference between the states $HH\pm$ at point D_1 , the transition to the $HH-$ state is incomplete, which is in contrast to the situation at point M_1 . The projection profile further demonstrates that the hole consists of both the states of $HH\pm$ during the cyclotron motion. Accordingly, the resulting trajectory is between the equienergy surfaces of $HH+$ and $HH-$ (Appendix A); e.g., from the point D_1 to D_2 in the second cycle, the hole has nearly an even ratio of the hybridization between $HH\pm$, and the trajectory is midway between two equienergy surfaces of $HH\pm$. When the hole passes point D_2 , the incomplete transition to $HH+$ prevents the hole trajectory from returning to the equienergy surface of $HH+$. Consequently, the cyclotron trajectory cannot be closed in a single cycle, and multi cycles are required.

We reinvestigate the distribution of the Abelian Berry curvature near the “dipole”-like singularity D [Fig. 9(a)]. In the $[1\bar{1}0]$ direction, we find the minimum point of the negative curvature at 22.4 meV, whereas the maximum point of the positive curvature is at 25.4 meV. We perform surface integration of the Abelian Berry curvature surrounded by the contour illustrated in Fig. 9(a); the negative area has a value of -0.04π and the positive area 0.05π . Thus these values of -0.04π and 0.05π cause the surface integral around point D to become negligible, which resulted in a “dipole”-like nature. In contrast, the corresponding surface integration around points Γ and M presents the values of 0.998π and -0.986π , respectively, and these points function as the “monopole”-like singularity.

We finally explore the features when the hole passes through these negative (22 meV) and positive (25 meV)

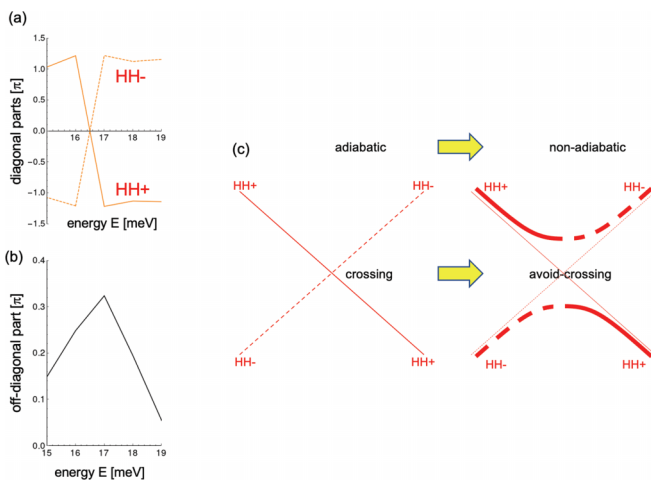


FIG. 6. Energy dependence of the non-Abelian Berry phase matrix for $HH\pm$ around the quasidegenerate points M ; diagonal elements (a) and off-diagonal elements (b). Schematic explanation for the discontinuity in the energy dependence of the non-Abelian Berry phase around the quasidegenerate points M (c).

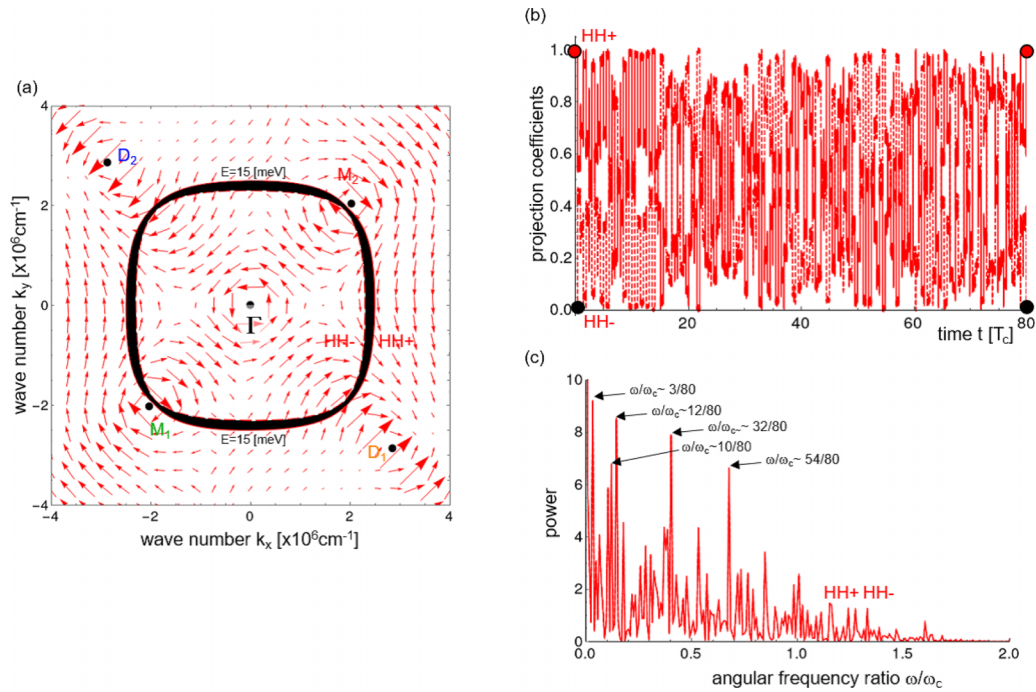


FIG. 7. k -space trajectory (black solid line) of the hole having an energy of 15 meV (a). We overwrite the vector-field distribution of the non-Abelian Berry connection (red arrows) and the equienergy surfaces (15 meV) of HH+ (red solid line) and HH- (red broken line). We illustrate the norm value of the in-plane vector by the arrow length in a logarithmic scale. We show the projection coefficients $|c_k^m|^2$ against time (b) and their Fourier components (c).

extrema. Figures 9(b) and 9(c) illustrate the trajectories of these holes having an energy of 22 and 25 meV, respectively. It should be noted that the cyclotron motion passing through the “monopole”-like point M requires a single cycle or a few cycles to close the cyclotron trajectory owing to the full-alternate transition. However, the above negative (22 meV)

and positive (25 meV) extrema deviate from point D , and the energy difference between HH \pm increases. Accordingly, the TD components of the hole interchange neither fully nor alternately owing to the reduced interstate transitions between these two states. Thus the closing of the trajectory requires multiple cycles of the cyclotron motion, as shown in Figs. 9(b)

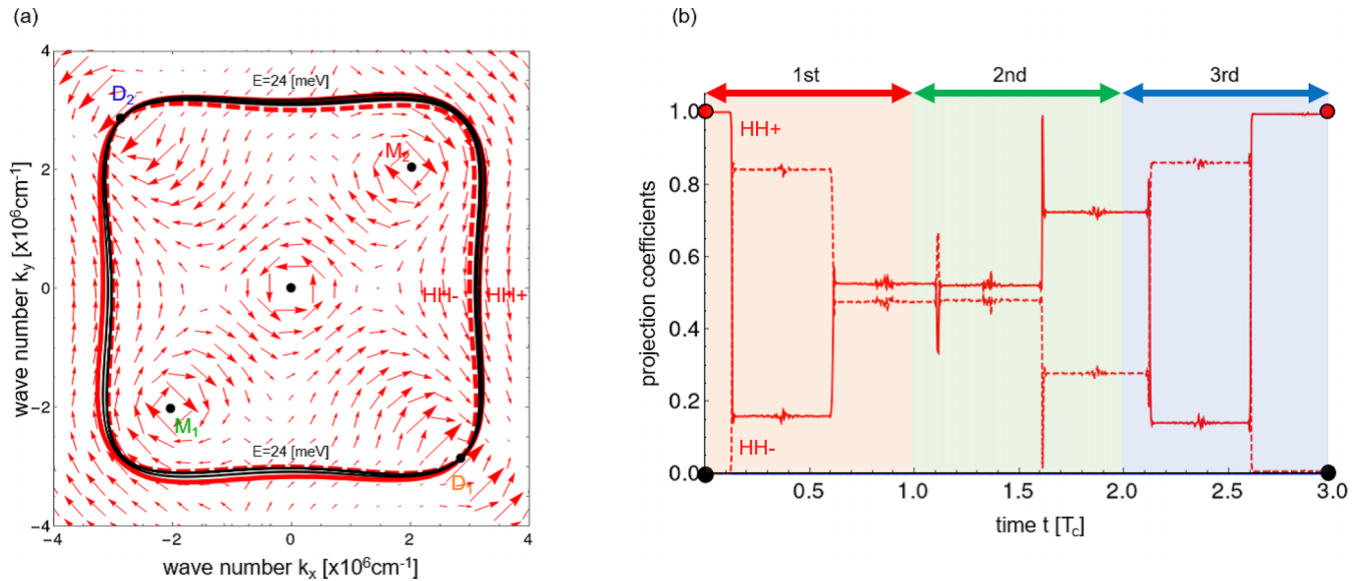


FIG. 8. k -space trajectory (black solid line) of the hole having a quasidegenerate energy of 24 meV while overwriting the non-Abelian Berry connection vector field (red arrows) and the equienergy surfaces (24 meV) of HH+ (red solid line) and HH- (red broken line) (a). We illustrate the norm value of the in-plane vector by the arrow length in a logarithmic scale. We present the projection coefficients $|c_k^m|^2$ against time (b). We indicate the first, second, and third cycles in red, green, and blue, respectively.

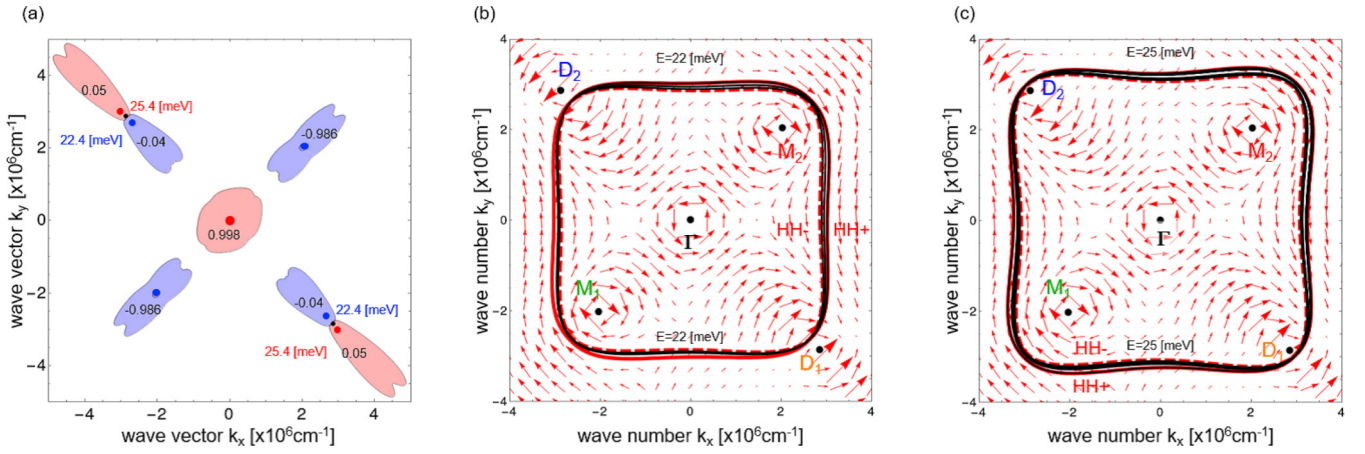


FIG. 9. k -space distribution of the Abelian Berry curvature for HH+ (a), and the resulting cyclotron trajectory (black solid line) of the hole having an energy of 22 (b) and 25 meV (c). We illustrate the contour of the Abelian Berry curvature of $\pm 1.0 \times 10^{-15} \text{ cm}^2$ in (a) and overwrite the vector field of the non-Abelian Berry connection (red arrows) and the equienergy surfaces of HH+ (red solid line) and HH- (red broken line) in (b) and (c). We illustrate the norm value of the in-plane vector by the arrow length in a logarithmic scale. [(a) is reproduced from our previous works [13,14] and partly modified. Copyright (2020) by Elsevier B. V., (2022) by Wiley-VCH GmbH.]

and 9(c), respectively. The weakened singularity around point D causes the “convex and dent” of the non-Abelian Berry phases, which is observed at approximately 21 and 26 meV in Fig. 3.

IV. SUMMARY

We formulated the non-Abelian Berry connection tensor \mathbb{R} and phase matrix Γ for the multiband system and applied them to semiconductor holes under the coexistence of the R- and D-type SOIs. We then calculated the energy dependence of Γ computationally while focusing on the HHs confined in $\text{Si}_{0.5}\text{Ge}_{0.5}$ 2DQW. We performed the contour integral of \mathbb{R} along the equienergy surface by combining the TD Schrödinger equation with the semiclassical equation of motion for the cyclotron motion.

The SOIs coupled strongly with ISI results in quasidegenerate states plurally around the semiconductor valence-band edge. These quasidegenerate points work as a Weyl-like singularity and cause π quantization in the energy dependence of the Berry phase under the adiabatic process. The nonadiabatic process induces intersubband hybridization, and the off-diagonal elements both in \mathbb{R} and Γ increase, in particular, around the quasidegenerate points. Consequently, the simple π quantization in the Berry phase is violated. More interestingly, the non-Abelian Berry phase for HH \pm interchanges mutually at the quasidegenerate energy of point M . Consequently, HH \pm exhibits a discontinuity in the energy dependence of Γ . This interchange-and-discontinuity can be explained by the interstate hybridization due to the nonadiabatic process, through which the off-diagonal terms are generated and the “resonant repulsion” is formed.

APPENDIX A: NON-ABELIAN BERRY CURVATURE

By employing the 2D non-Abelian Berry connection tensor $\mathbb{R}_{mm'}^{\xi}$ of Eq. (5), the out-of-plane component of the

non-Abelian Berry curvature matrix $\Omega_{mm'}^z$ is given by [23,28]

$$\begin{aligned} \Omega_{mm'}^z(\mathbf{k}) &= [\nabla_{\mathbf{k}} \times \mathbb{R}_{mm'}(\mathbf{k})]_z - i \sum_l [\mathbb{R}_{ml}(\mathbf{k}) \times \mathbb{R}_{lm'}(\mathbf{k})]_z \\ &= \left(\frac{\partial \mathbb{R}_{mm'}^y(\mathbf{k})}{\partial k_x} - \frac{\partial \mathbb{R}_{mm'}^x(\mathbf{k})}{\partial k_y} \right) \\ &\quad - i \sum_l (\mathbb{R}_{ml}^x(\mathbf{k}) \mathbb{R}_{lm'}^y(\mathbf{k}) - \mathbb{R}_{ml}^y(\mathbf{k}) \mathbb{R}_{lm'}^x(\mathbf{k})). \end{aligned} \quad (\text{A1})$$

We further define the symbols $\Omega_{mm'}^{(1)z}(\mathbf{k})$ and $\Omega_{mm'}^{(2)z}(\mathbf{k})$ as

$$\begin{aligned} \Omega_{mm'}^{(1)z}(\mathbf{k}) &\equiv [\nabla_{\mathbf{k}} \times \mathbb{R}_{mm'}(\mathbf{k})]_z = \frac{\partial \mathbb{R}_{mm'}^y(\mathbf{k})}{\partial k_x} - \frac{\partial \mathbb{R}_{mm'}^x(\mathbf{k})}{\partial k_y}, \\ \Omega_{mm'}^{(2)z}(\mathbf{k}) &\equiv -i \sum_l [\mathbb{R}_{ml}(\mathbf{k}) \times \mathbb{R}_{lm'}(\mathbf{k})]_z \\ &= -i \sum_l [\mathbb{R}_{ml}^x(\mathbf{k}) \mathbb{R}_{lm'}^y(\mathbf{k}) - \mathbb{R}_{ml}^y(\mathbf{k}) \mathbb{R}_{lm'}^x(\mathbf{k})]. \end{aligned} \quad (\text{A2})$$

Accordingly, the out-of-plane component Eq. (A1) is decomposed into

$$\Omega_{mm'}^z(\mathbf{k}) \equiv \Omega_{mm'}^{(1)z}(\mathbf{k}) + \Omega_{mm'}^{(2)z}(\mathbf{k}). \quad (\text{A3})$$

Because the non-Abelian Berry curvature has a matrix form $\Omega_{mm'}^z(\mathbf{k})$ owing to the nonadiabatic process, we cannot compare the non-Abelian result with the Abelian one in a straightforward manner. We therefore focus on the diagonal elements of $\Omega_{mm}^{(1)z}(\mathbf{k})$ and $\Omega_{mm}^{(2)z}(\mathbf{k})$ and investigate the influence of the nonadiabatic process on the diagonal elements. Figure 10(a) presents the diagonal elements of $\Omega_{mm}^{(1)z}(\mathbf{k})$. The comparison of Fig. 10(a) with Fig. 9(a) reveals that the diagonal component $\Omega_{mm}^{(1)z}(\mathbf{k})$ coincides with the Abelian Berry curvature because the diagonal element $\Omega_{mm}^{(1)z}(\mathbf{k})$ can be rewritten as

$$\begin{aligned} \Omega_{mm}^{(1)z}(\mathbf{k}) &= \frac{\partial \mathbb{R}_{mm}^y(\mathbf{k})}{\partial k_x} - \frac{\partial \mathbb{R}_{mm}^x(\mathbf{k})}{\partial k_y} \\ &= \frac{\partial A_m^y(\mathbf{k})}{\partial k_x} - \frac{\partial A_m^x(\mathbf{k})}{\partial k_y} = B_m^z(\mathbf{k}). \end{aligned} \quad (\text{A4})$$

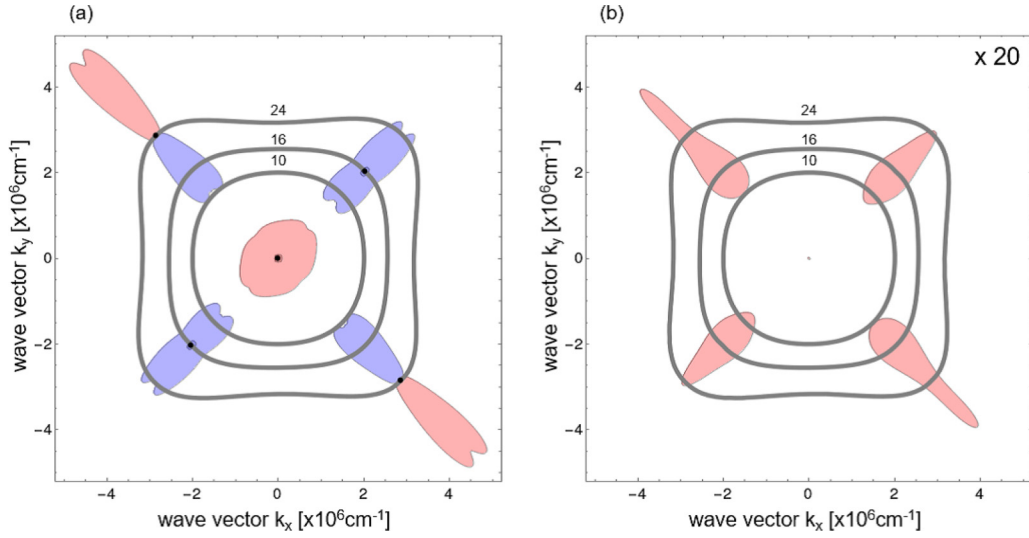


FIG. 10. k space distribution of the in-plane diagonal component of the non-Abelian Berry curvature for HH+: $\Omega_{mm}^{(1)z}(\mathbf{k})$ (a) and $\Omega_{mm}^{(2)z}(\mathbf{k})$ (b).

Here, $A_m^\xi(\mathbf{k})$ denotes the Abelian Berry connection for the m th hole, as defined in Eq. (7). As such, the diagonal element $\Omega_{mm}^{(1)z}(\mathbf{k})$ represents the out-of-plane (z) component of the Abelian Berry curvature, which indicates complete coincidence between Figs. 10(a) and 9(a).

The sum over the interstates in Eq. (A2) demonstrates that the second term $\Omega_{mm'}^{(2)z}(\mathbf{k})$ of Eq. (A3) represents the influence of the interstate transition due to the nonadiabatic process. In the present work, we have a particular interest in how the ISI via a nonadiabatic process modifies even the diagonal element of the non-Abelian Berry curvature. Accordingly, we obtain the sum l over other hole states (LHs and SHs) and calculate the distribution of $\Omega_{mm}^{(2)z}(\mathbf{k})$ [Fig. 10(b)]. As the resulting values are small, we magnify them by 20 times to perform a comparison with $\Omega_{mm}^{(1)z}(\mathbf{k})$. In the lower-energy region of less than 10 meV, $\Omega_{mm}^{(2)z}(\mathbf{k})$ does not provide any meaningful values. This is why the non-Abelian Berry phase in such a lower-energy region is not influenced much by the nonadiabatic process. With an increase in energy, the nonadiabatic process causes intersubband hybridization, especially around the quasidegenerate points M and D . Thus small but meaningful values are produced in the $\langle 110 \rangle$ and $\langle 1\bar{1}0 \rangle$ directions [Fig. 10(b)]. Eventually, the nonadiabatic process has an influence *even on* the diagonal component of the non-Abelian Berry curvature via $\Omega_{mm}^{(2)z}(\mathbf{k})$.

APPENDIX B: CALCULATION DETAILS IN NON-ABELIAN BERRY PHASE

1. Time-ordered product

We rewrite Eq. (3) into its vector representation as

$$\frac{d\mathbf{c}_k}{dt} = i \left(\sum_{\xi} \mathbb{R}^{\xi}(\mathbf{k}) \dot{k}_{\xi} - \frac{\Xi \mathbf{k}}{\hbar} \right) \mathbf{c}_k, \quad (\text{B1})$$

where we represent the expansion coefficient vector \mathbf{c}_k as

$$\mathbf{c}_k = \begin{pmatrix} c_k^1 \\ c_k^2 \\ \vdots \\ c_k^N \end{pmatrix}. \quad (\text{B2})$$

In order to eliminate the dynamical term explicitly from the time-dependent process, we define the expansion coefficient vector $\mathbf{c}'_k(t)$ as

$$\mathbf{c}'_k(t) = e^{i \int_0^t \Xi_{k(t')} dt' / \hbar} \mathbf{c}_k(t). \quad (\text{B3})$$

Thus the rate equation (B1) is rewritten as

$$\frac{d\mathbf{c}'_k}{dt} = i \sum_{\xi} \bar{\mathbb{R}}^{\xi}(\mathbf{k}) \dot{k}_{\xi} \mathbf{c}'_k. \quad (\text{B4})$$

Here, we define the rationalized non-Abelian Berry connection tensor $\bar{\mathbb{R}}_{mm'}^{\xi}(\mathbf{k})$ as

$$\begin{aligned} \bar{\mathbb{R}}_{mm'}^{\xi}(\mathbf{k}) &= \exp \left[i \int_0^t \frac{E_{k(t')}^m - E_{k(t')}^{m'}}{\hbar} dt' \right] \mathbb{R}_{mm'}^{\xi}(\mathbf{k}) \\ &= i \exp \left[i \int_0^t \frac{E_{k(t')}^m - E_{k(t')}^{m'}}{\hbar} dt' \right] \left\langle u_{\mathbf{k}}^m \left| \frac{\partial u_{\mathbf{k}}^{m'}}{\partial k_{\xi}} \right. \right\rangle. \end{aligned} \quad (\text{B5})$$

The tensor $\bar{\mathbb{R}}_{mm'}^{\xi}(\mathbf{k})$ is further simplified when eigenstates $|u_{\mathbf{k}}^m\rangle$ and $|u_{\mathbf{k}}^{m'}\rangle$ are not degenerate, i.e., $E_{\mathbf{k}}^m \neq E_{\mathbf{k}}^{m'}$;

$$\bar{\mathbb{R}}_{mm'}^{\xi}(\mathbf{k}) = \begin{cases} i \langle u_{\mathbf{k}}^m | \frac{\partial}{\partial k_{\xi}} | u_{\mathbf{k}}^m \rangle & (m = m') \\ -i \exp \left[i \int_0^t \frac{E_{k(t')}^m - E_{k(t')}^{m'}}{\hbar} dt' \right] \frac{\langle u_{\mathbf{k}}^m | \frac{\partial}{\partial k_{\xi}} \mathcal{H}_{\mathbf{k}} | u_{\mathbf{k}}^{m'} \rangle}{E_{\mathbf{k}}^m - E_{\mathbf{k}}^{m'}} & (m \neq m'). \end{cases} \quad (\text{B6})$$

The employment of the time-ordered product \mathcal{T} for $\bar{\mathbb{R}}^\xi(\mathbf{k})$ allows us to obtain the formal solution of the rate equation (B4):

$$\mathbf{c}'_k(T_{\text{cls}}) = \mathcal{T} \exp \left[i \int_0^{T_{\text{cls}}} \sum_{\xi} \bar{\mathbb{R}}^\xi(\mathbf{k}) \dot{k}_{\xi} dt \right] \mathbf{c}'_k(0) \equiv \exp(iN_{\text{cyc}} \mathbf{\Gamma}) \mathbf{c}'_k(0). \quad (\text{B7})$$

Thus we can determine the non-Abelian Berry phase tensor $\mathbf{\Gamma}$ as

$$\mathbf{\Gamma} = -\frac{i}{N_{\text{cyc}}} \ln \left(\mathcal{T} \exp \left[i \int_0^{T_{\text{cls}}} \sum_{\xi} \bar{\mathbb{R}}^\xi(\mathbf{k}) \dot{k}_{\xi} dt \right] \right). \quad (\text{B8})$$

2. Application of Crank–Nicolson method

In Eq. (16), we have $U(t + \Delta t)$, which has a short-time proceeding Δt

$$\begin{aligned} U(t + \Delta t) &= \mathcal{T} \exp \left[i \sum_{\xi} \int_0^{t+\Delta t} \bar{\mathbb{R}}^\xi \dot{k}_{\xi}(E) dt' \right] \\ &= \mathcal{T} \exp \left[i \sum_{\xi} \int_t^{t+\Delta t} \bar{\mathbb{R}}^\xi \dot{k}_{\xi}(E) dt' \right] \mathcal{T} \exp \left[i \sum_{\xi} \int_0^t \bar{\mathbb{R}}^\xi \dot{k}_{\xi}(E) dt' \right] \\ &= \mathcal{T} \exp \left[i \sum_{\xi} \int_t^{t+\Delta t} \bar{\mathbb{R}}^\xi \dot{k}_{\xi}(E) dt' \right] U(t). \end{aligned} \quad (\text{B9})$$

We further divide the short-time period Δt into halves:

$$U(t + \Delta t) = \mathcal{T} \exp \left[i \sum_{\xi} \int_{t+\Delta t/2}^{t+\Delta t} \bar{\mathbb{R}}^\xi \dot{k}_{\xi}(E) dt' \right] \mathcal{T} \exp \left[i \sum_{\xi} \int_t^{t+\Delta t/2} \bar{\mathbb{R}}^\xi \dot{k}_{\xi}(E) dt' \right] U(t). \quad (\text{B10})$$

Accordingly, we obtain the following relation:

$$\left(\mathcal{T} \exp \left[i \sum_{\xi} \int_{t+\Delta t/2}^{t+\Delta t} \bar{\mathbb{R}}^\xi \dot{k}_{\xi}(E) dt' \right] \right)^{-1} U(t + \Delta t) = \mathcal{T} \exp \left[i \sum_{\xi} \int_t^{t+\Delta t/2} \bar{\mathbb{R}}^\xi \dot{k}_{\xi}(E) dt' \right] U(t). \quad (\text{B11})$$

The Crank–Nicolson approach employs the first-order Taylor expansion for the time-ordered product at $t + \Delta t/2$.

$$U(t + \Delta t) = \left(I - i \sum_{\xi} \bar{\mathbb{R}}^\xi(t + \Delta t/2) \dot{k}_{\xi}(t + \Delta t/2) \frac{\Delta t}{2} \right)^{-1} \left(I + i \sum_{\xi} \bar{\mathbb{R}}^\xi(t + \Delta t/2) \dot{k}_{\xi}(t + \Delta t/2) \frac{\Delta t}{2} \right) U(t). \quad (\text{B12})$$

Thus we can determine $U(t)$ at any time t by setting the initial condition as $U(0) = I$.

In the practical calculation, we focus our attention on the unitarity of the matrix $U(t)$ because Eq. (B12) has a unitary operation. We divide the \mathbf{k} space into the line element of $dk \sim 1 \times 10^3 \text{ cm}^{-1}$. Accordingly, the time-ordered product along the equienergy surface (e.g., $E = 10 \text{ meV}$) requires the calculation of 13 550 000 steps. We executed the present numerical calculations of the total energy with an accuracy within an error of less than $1 \times 10^{-6} \%$ to confirm that the energy is conserved during the ‘‘cyclotron motion.’’ Owing to the matrix form of the non-Abelian Berry phase $\mathbf{\Gamma}$ [Eq. (10)], we diagonalize it and identify the eigenvalues of $\text{HH}\pm$, $\text{LH}\pm$, and $\text{SH}\pm$, respectively, based on the components $|yz\rangle$, $|zx\rangle$, and $|xy\rangle$ including a spin.

-
- [1] D. J. Thouless, M. Kohmoto, M. P. Nightingale, and M. den Nijs, *Phys. Rev. Lett.* **49**, 405 (1982).
[2] M. Kohmoto, *Ann. Phys.* **160**, 343 (1985).
[3] J. C. Solem and L. C. Biedenharn, *Found. Phys.* **23**, 185 (1993).
[4] K. S. Novoselov, A. K. Geim, S. V. Morozov, D. Jiang, Y. Zhang, S. V. Dubonos, I. V. Grigorieva, and A. A. Firsov, *Science* **306**, 666 (2004).
[5] K. S. Novoselov, A. K. Geim, S. V. Morozov, D. Jiang, M. I. Katsnelson, I. V. Grigorieva, S. V. Dubonos, and A. A. Firsov, *Nature (London)* **438**, 197 (2005).
[6] G. P. Mikitik and Y. V. Sharlai, *Phys. Rev. Lett.* **82**, 2147 (1999).
[7] I. A. Luk'yanchuk and Y. Kopelevich, *Phys. Rev. Lett.* **93**, 166402 (2004).
[8] M. V. Berry, *Proc. R. Soc. London A* **392**, 45 (1984).
[9] S.-S. Chern and J. Simons, *Ann. Math.* **99**, 48 (1974).
[10] Y. Zhang, Y.-W. Tan, H. L. Stormer, and P. Kim, *Nature (London)* **438**, 201 (2005).
[11] E. I. Rashba, *Sov. Phys. Solid State* **2**, 1109 (1960).
[12] G. Dresselhaus, *Phys. Rev.* **100**, 580 (1955).

- [13] T. Tojo and K. Takeda, *Phys. Lett. A* **389**, 127091 (2021).
- [14] T. Tojo and K. Takeda, *Phys. Status Solidi B* **260**, 2200319 (2023).
- [15] R. Winkler, *Spin-Orbit Coupling Effects in Two-Dimensional Electron and Hole Systems* (Springer, Berlin, 2003).
- [16] R. Winkler, *Phys. Rev. B* **71**, 113307 (2005).
- [17] R. Winkler, D. Culcer, S. J. Papadakis, B. Habib, and M. Shayegan, *Semicond. Sci. Technol.* **23**, 114017 (2008).
- [18] D. Culcer, C. Lechner, and R. Winkler, *Phys. Rev. Lett.* **97**, 106601 (2006).
- [19] R. Winkler, *Phys. Rev. B* **62**, 4245 (2000).
- [20] S. D. Ganichev and L. E. Golub, *Phys. Status Solidi B* **251**, 1801 (2014).
- [21] Y. Hatsugai, *Suuri Kagaku (Mathematical Science)* **528**, 26 (2007), in Japanese.
- [22] F. Wilczek and A. Zee, *Phys. Rev. Lett.* **52**, 2111 (1984).
- [23] L.-k. Shi, S.-C. Zhang, and K. Chang, *Phys. Rev. B* **87**, 161115(R) (2013).
- [24] J. Pachos, P. Zanardi, and M. Rasetti, *Phys. Rev. A* **61**, 010305(R) (1999).
- [25] M. M. Wysockiński, M. Płodzień, and M. Trif, *Phys. Rev. B* **104**, L041402 (2021).
- [26] H. Weisbrich, R. L. Klees, G. Rastelli, and W. Belzig, *PRX Quantum* **2**, 010310 (2021).
- [27] C. Zu, W.-B. Wang, L. He, W.-G. Zhang, C.-Y. Dai, F. Wang, and L.-M. Duan, *Nature (London)* **514**, 72 (2014).
- [28] M.-C. Chang and Q. Niu, *J. Phys.: Condens. Matter* **20**, 193202 (2008).
- [29] G. Dresselhaus, A. F. Kip, and C. Kittel, *Phys. Rev.* **98**, 368 (1955).
- [30] T. Tojo and K. Takeda, *J. Phys. Soc. Jpn.* **88**, 094711 (2019).
- [31] T. Tojo, K. Tsuruta, Y. Takahashi, and K. Takeda, *J. Phys.: Condens. Matter* **32**, 095302 (2020).
- [32] See Supplemental Material at <http://link.aps.org/supplemental/10.1103/PhysRevB.108.125432> for (A) “extended $k \cdot p$ Approach” and (B) “calculational remarks,” which includes Refs. [33–46].
- [33] W. Shockley, *Electrons and Holes in Semiconductors* (D. van Nostrand Company, New York, 1950).
- [34] R. H. Parmenter, *Phys. Rev.* **100**, 573 (1955).
- [35] J. M. Luttinger and W. Kohn, *Phys. Rev.* **97**, 869 (1955).
- [36] J. M. Luttinger, *Phys. Rev.* **102**, 1030 (1956).
- [37] E. O. Kane, *J. Phys. Chem. Solids* **1**, 249 (1957); **1**, 82 (1956) for group IV semiconductors.
- [38] G. Kusumoto and K. Kurata, *J. Crystallogr. Soc. Jpn.* **12**, 200 (1970), in Japanese.
- [39] T. Naito, M. Yamada, M. Tsukahara, S. Yamada, K. Sawano, and K. Hamaya, *Appl. Phys. Express* **11**, 053006 (2018).
- [40] K. Lai, T. M. Lu, W. Pan, D. C. Tsui, S. Lyon, J. Liu, Y. H. Xie, M. Mühlberger, and F. Schäffler, *Phys. Rev. B* **73**, 161301(R) (2006).
- [41] K. Lai, W. Pan, D. C. Tsui, S. Lyon, M. Mühlberger, and F. Schäffler, *Phys. Rev. Lett.* **93**, 156805 (2004).
- [42] K. Hamaya, K. Sugihara, H. Takahashi, S. Masubuchi, M. Kawamura, T. Machida, K. Sawano, and Y. Shiraki, *Phys. Rev. B* **75**, 033307 (2007).
- [43] K. Hamaya, S. Masubuchi, K. Hirakawa, S. Ishida, Y. Arakawa, K. Sawano, Y. Shiraki, and T. Machida, *Phys. Rev. B* **73**, 121304(R) (2006).
- [44] R. Vrijen, E. Yablonovitch, K. Wang, H. W. Jiang, A. Balandin, V. Roychowdhury, T. Mor, and D. DiVincenzo, *Phys. Rev. A* **62**, 012306 (2000).
- [45] K. Takeda, A. Taguchi, and M. Sakata, *J. Phys. C: Solid State Phys.* **16**, 2237 (1983).
- [46] K. Sato, T. Tojo, and K. Takeda, *JPS Conf. Proc.* **38**, 011016 (2023).
- [47] I. Berbezier and A. Ronda, *Surf. Sci. Rep.* **64**, 47 (2009).
- [48] Y. Shiraki and A. Sakai, *Surf. Sci. Rep.* **59**, 153 (2005).
- [49] A. Wolos, Z. Wilamowski, C. Skierbiszewski, A. Drabinska, B. Lucznik, I. Grzegory, and S. Porowski, *Phys. B: Condens. Matter* **406**, 2548 (2011).
- [50] Y. Zhang, F. Xue, C. Tang, J. Li, L. Liao, L. Li, X. Liu, Y. Yang, C. Song, and X. Kou, *ACS Nano* **14**, 17396 (2020).
- [51] M. Studer, M. P. Walser, S. Baer, H. Rusterholz, S. Schön, D. Schuh, W. Wegscheider, K. Ensslin, and G. Salis, *Phys. Rev. B* **82**, 235320 (2010).
- [52] M. Reine, R. L. Aggarwal, B. Lax, and C. M. Wolfe, *Phys. Rev. B* **2**, 458 (1970).
- [53] J. S. Sheng and K. Chang, *Phys. Rev. B* **74**, 235315 (2006).
- [54] Although the 2D quantum structure breaks the symmetry of the T_d crystal potential, the 2D quantum plane has sufficient thickness to neglect such structural breaking.
- [55] N. A. Sinitsyn, A. H. MacDonald, T. Jungwirth, V. K. Dugaev, and J. Sinova, *Phys. Rev. B* **75**, 045315 (2007).